Electronic Supplementary Material (ESI) for Inorganic Chemistry Frontiers.

Supporting Information

Molten-Salt-Induced Phosphorus Vacancy Defect Engineering of Heterostructured Cobalt Phosphide for Efficient Overall Water Splitting

Zhida Li, Chunyue Zhang, Yang Yang, Shanshan Pi, Yongjie Yu, Chengfeng Wan, Baiqin Zhou, Weixiang Chao, Lu Lu*

State Key Laboratory of Urban Water Resource and Environment, School of Civil and Environmental Engineering, Harbin Institute of Technology, Shenzhen 518055, China

Corresponding email: lulu@hit.edu.cn

1. Experimental Section

1.1 Characterization of CoP_x

Structural features of CoP_x were revealed by Scanning Electron Microscope (SEM) and Transmission Electron Microscope (TEM). SEM images were obtained with an acceleration voltage of 5 kV, while energy dispersive spectroscopy (EDS) data were acquired with an acceleration voltage of 15 kV. TEM imaging was performed on FEI Tecnai G2 F30 equipped with an EDS detector at an acceleration voltage of 200 kV. XRD patterns were examined by Panalytical Aries with Cu-Kα radiation (λ = 1.5406 Å) at 40 kV and 15 mA with a scan step size of 0.0217. X-ray photoelectron spectroscopy (XPS) was conducted on a Thermo Scientific™ K-Alpha™+ spectrometer equipped with a monochromatic Al Kα X-ray source (1486.6 eV) operating at 100 W. Samples were analyzed under vacuum ($P < 10^{-8}$ mbar) with a pass energy of 150 eV (survey scans) or 30 eV (high-resolution scans). The obtained XPS spectra were fitted with XPS peak software to analyze all chemical compositions. The binding energy was calibrated using the C 1s peak at 284.6 eV.[1] Raman spectra were tested by RENISHAW inVia Raman microscope with an Ar-ion laser operating at 532 nm. EPR spectra were recorded on a Bruker EMX spectrometer (X-band) operating at a frequency of ~9.46 GHz.

1.2 Electrochemical Characterization

1.2.1 Working electrode preparation

To prepare the working electrode, 10 mg electrocatalyst was firstly dispersed into 1 mL ethanol containing 50 μL Nafion solution (5 wt%) with the aid of bath sonication (15 min) to form the standby homogeneous ink suspension. Afterwards, 25 μL ink suspension was loaded onto a CFP with a surface area of 0.5*2 cm (repeat for 4 times) dropwise, which was then dried under room temperature for about 2 hours. The loading amount of CoP_x on CFP is about 1.0 mg cm^{-2}. To compare with the HER activity of CoP_x, Pt/C (20%) working electrode was

prepared. 5 mg commercial 20% Pt/C powders were dispersed into 1 mL ethanol plus 50 μL Nafion solution under bath sonication (15 min), and then 25 μL Pt/C ink suspension was loaded onto 0.5*2 cm CFP dropwise. For comparison with the OER activity of CoP_x, IrO_2 supported on Ti mesh was prepared according to a previous paper.[2] A Ti mesh was firstly washed by 85 ^oC 6 M HCl solution to remove the surface impurities. Then 1 mL $H_2IrCl_6 \cdot xH_2O$ solution (10 mg $H_2IrCl_6 \cdot xH_2O$ dissolved in 900 μL isopropanol and 100 μL 6 M HCl) was dispersed onto the Ti mesh by drop casting, which was subsequently heated under 100 ^oC for 10 min. The loading amount of $H_2IrCl_6 \cdot xH_2O$ on Ti mesh is approximate 2 mg cm^{-2}. The dried Ti mesh was finally calcinated under 500 ^oC for 10 min to give rise to IrO_2 formation.

1.2.2 Electrochemical measurements

Electrochemical measurements were firstly carried out in 1 M KOH solution saturated with N_2 within a standard three-electrode configuration, where graphite rod was used as counter electrode, and SCE (saturated calomel electrode) was employed as reference electrode. All potentials in this work were converted to reversible hydrogen electrode (RHE) by the equation of: $E_{RHE} = E_{apply} + 0.24\ V + 0.0592 * pH$. Before formal electrochemical tests, continuous cyclic voltammetry (CV) scans were conducted until a stable and reproducible CV curve was obtained. The polarization curves (linear sweep voltammograms, LSV) were recorded with a scanning rate of 5 mV s^{-1}. The electrochemical impedance spectra (EIS) were tested with an overpotential of 100 mV (HER) and 300 mV (OER) within the frequency range of 0.1 to 10^5 Hz. Electrochemical active surface area (ECSA) was evaluated by calculating the electrochemical double-layer capacitances (C_{dl}) derived from CV results. CV was measured with varying scanning rates of 20, 40, 60, 80 and 100 mV s^{-1} within the potential range of 0.1 to 0.2 V vs RHE. For overall water splitting experiments, the optimal MS-CoP_x-350 was used to assemble MS-CoP_x-350|| MS-CoP_x-350 electrolyzer. Polarization curve was obtained by applying a cell

voltage from 0 to 2 V with a scanning rate of 5 mV s^{-1}; stability was evaluated by applying a constant current density of 100 mA cm^{-2} to the assembled electrolyzer.

HER performance of CoP_x was further measured in N_2-saturated 0.5 M H_2SO_4 within a three-electrode configuration. Graphite rod and Ag/AgCl (3 M NaCl) were used as the counter and reference electrode, respectively. Polarization curves were obtained using a scanning rate of 5 mV s^{-1}. Potentials were then converted to reversible hydrogen electrode (RHE) by the equation of: $E_{RHE} = E_{apply} + 0.21\ V + 0.0592 * pH$.

1.3 Density of Functional Theory (DFT) Calculations

In this work, VASP [3, 4] was employed to perform DFT calculations within the generalized gradient approximation (GGA) according to the Perdew-Burke-Ernzerhof (PBE) [5] formulation. The projected augmented wave (PAW) potentials [6] were chosen to describe the ionic cores. Valence electrons were taken into account by a plane wave basis set with a kinetic energy cutoff of 450 eV. Partial occupancies of the Kohn-Sham orbitals were allowed with Gaussian smearing method and a width of 0.05 eV. The electronic energy was considered self-consistent when the energy change was smaller than 10^{-5} eV; a geometry optimization was thought to be convergent when the energy change was smaller than 0.05 eV $Å^{-1}$. The Brillourin zone was sampled with a gamma-centered grid 1× 1× 1 for all computational process.[7]

The free energy (ΔG) of OER on catalysts was defined as:[8]

$$\Delta G = E\ (\mathrm{DFT}) + \Delta E\ (\mathrm{ZPE}) - T\Delta S \quad (1)$$

Where E (DFT) is the total energy for the adsorption OOH* OH* and O*; ΔE (ZPE) is the zero-point energy change; ΔS is the entropy change.

2. Results and Discussion

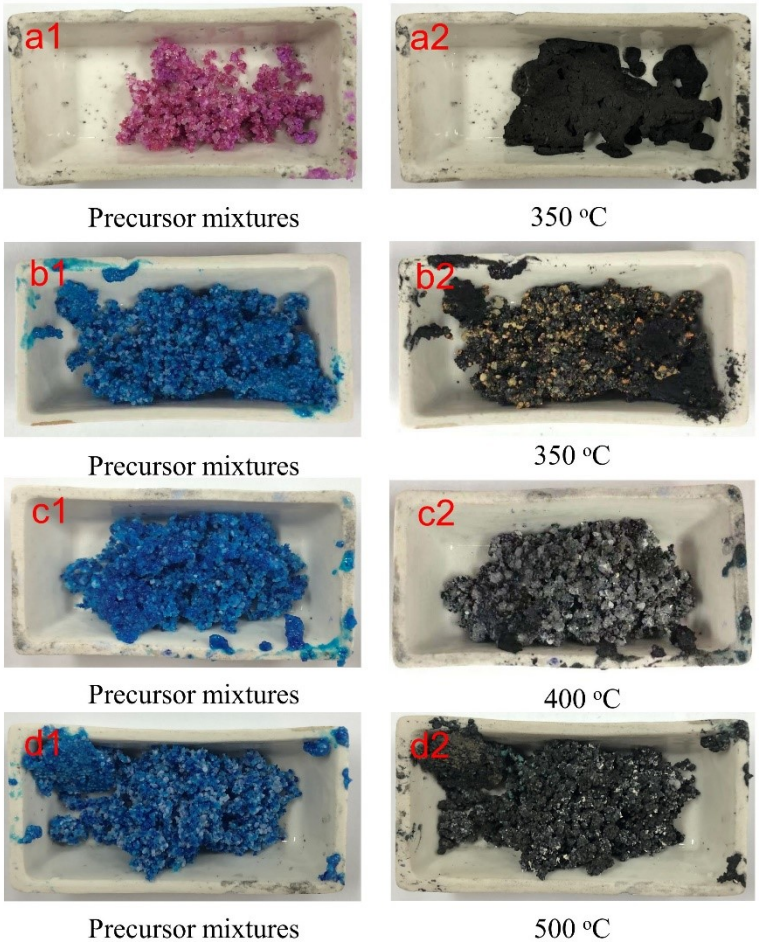

Fig. S1 Digital graphs of precursor mixtures and corresponding products. (a) CoP_x-350, (b) MS-CoP_x-350, (c) MS-CoP_x-400 and (d) MS-CoP_x-500.

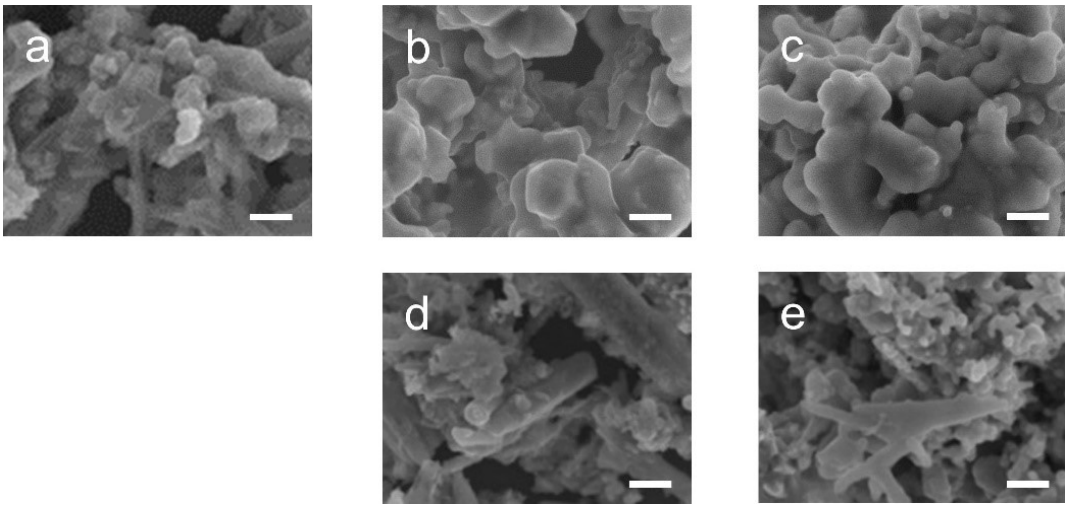

Fig. S2 SEM graphs of (a) CoP_x-350, (b) CoP_x-400, (c) CoP_x-500, (d) MS-CoP_x-400, (e) MS-CoP_x-500.

CoP_x prepared withou molten salt (Fig. S2, a-c) show amorphous and compact structure. By comparison, samples acquired within molten salt (Fig. S2, d-e) exhibit a mixture of nanoparticles and nanorods.

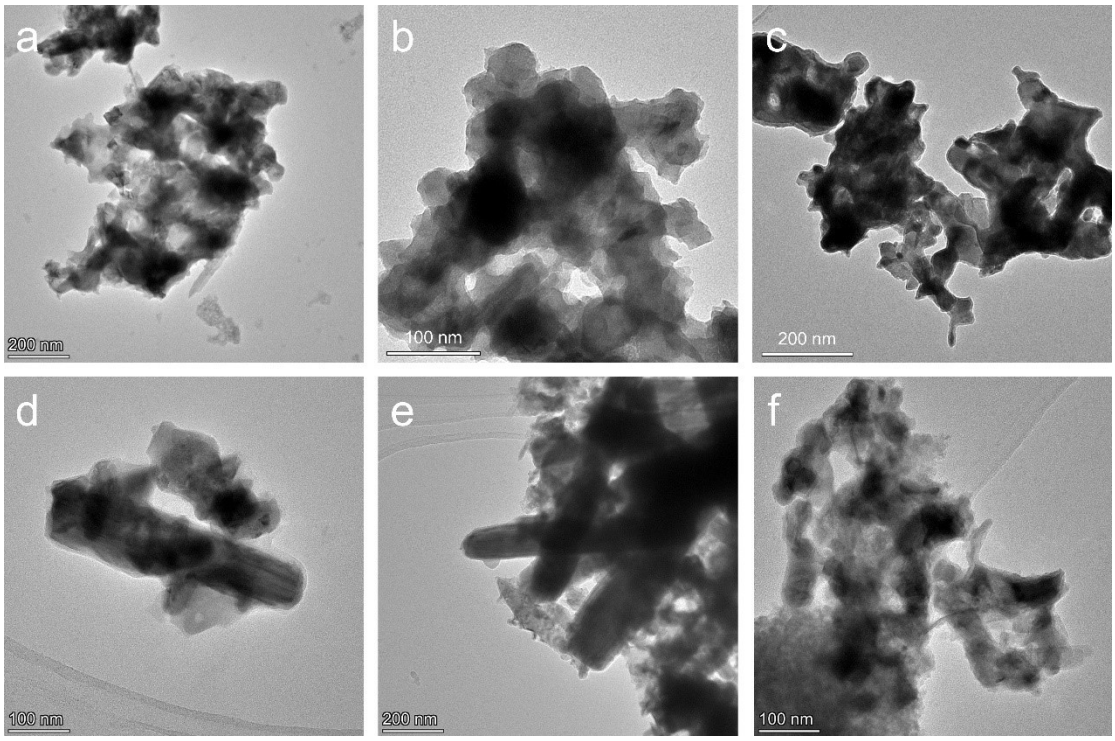

Fig. S3 TEM images of CoP_x prepared under different conditions. (a) CoP_x-350, (b) CoP_x-400, (c) CoP_x-500, (d) MS-CoP_x-350, (e) MS-CoP_x-400, (f) MS-CoP_x-500.

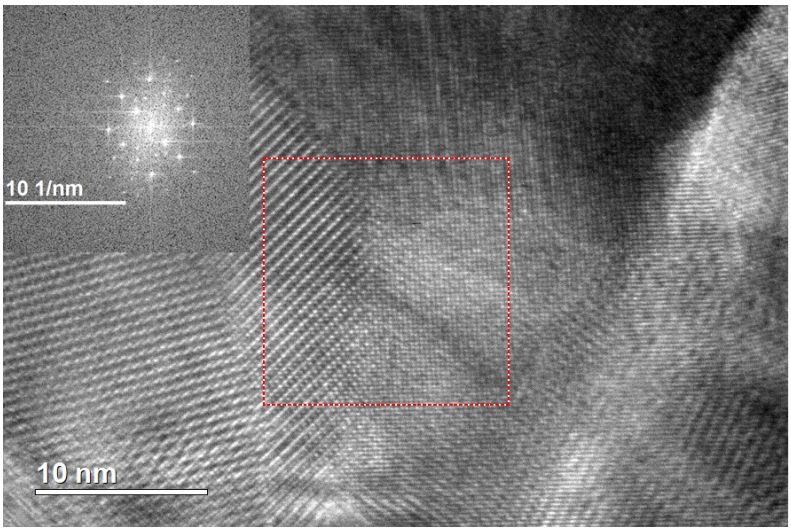

Fig. S4 HRTEM and corresponding FFT graphs of MS-CoP_x-350.

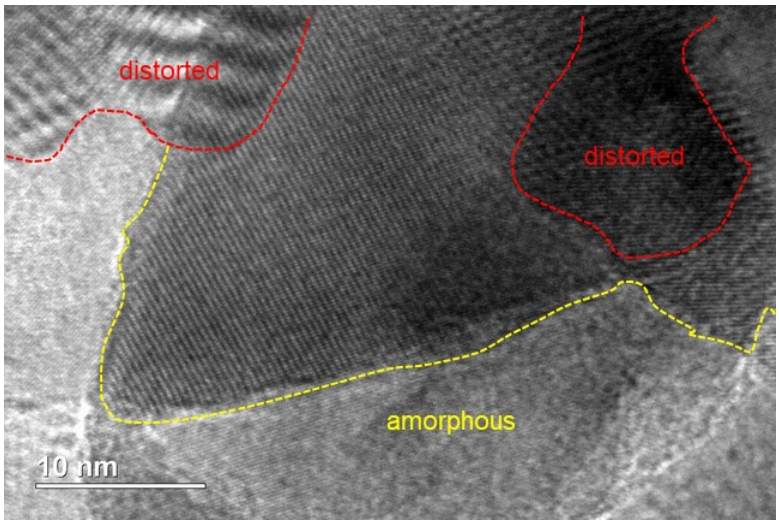

Fig. S5 HRTEM image of MS-CoP_x-350. One can observe the distorted regions and amorphous regions from this image. Together with Fig. S4, these TEM data evidence that MS-CoP_x-350 is polycrystalline. Further, the distorted and amorphous regions might contribute to more active sites' exposure, thus resulting in a boosted electrochemical activity.

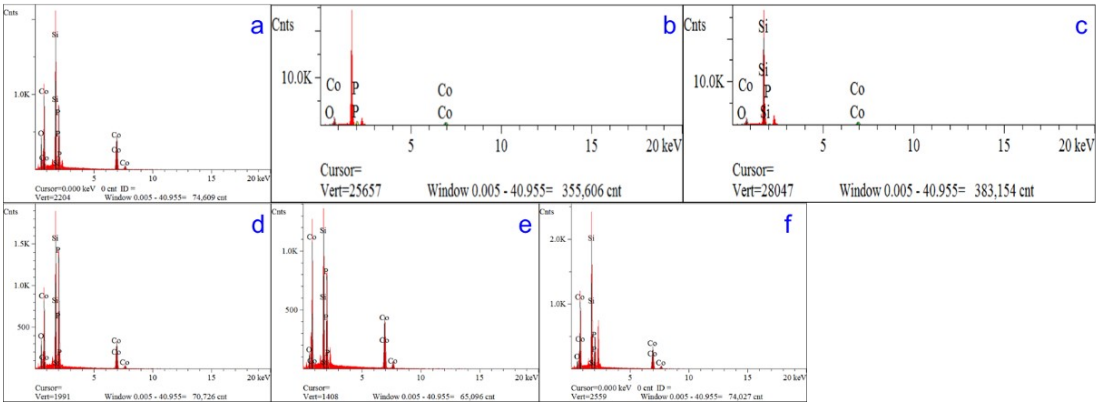

Fig. S6 EDS spectra of CoP_x. (a) CoP_x-350, (b) CoP_x-400, (c) CoP_x-500, (d) MS-CoP_x-350, (e) MS-CoP_x-400, (f) MS-CoP_x-500. Si signal was derived from the Si substrate. To prepare SEM-EDS samples, CoP_x was dispersed into ethanol to form homogeneous solution with the aid of bath sonication. Then 1 drop of solution (~10 μL) was loaded onto Si substrate.

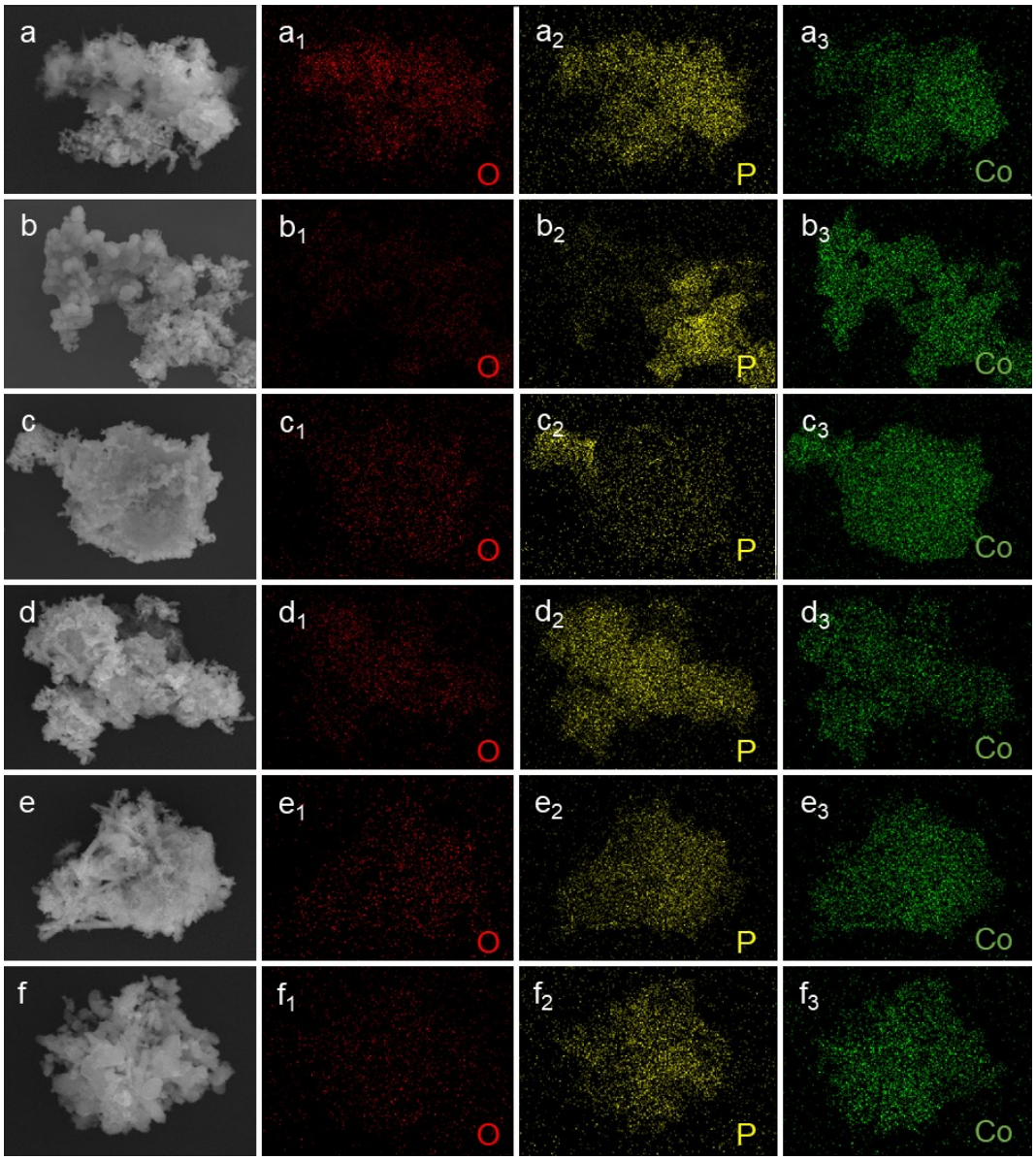

Fig. S7 EDS mappings of CoP_x. (a) CoP_x-350, (b) CoP_x-400, (c) CoP_x-500, (d) MS-CoP_x-350, (e) MS-CoP_x-400, (f) MS-CoP_x-500. O, P and Co are uniformly distributed, suggesting the formation of CoP_x with some surface oxidation.

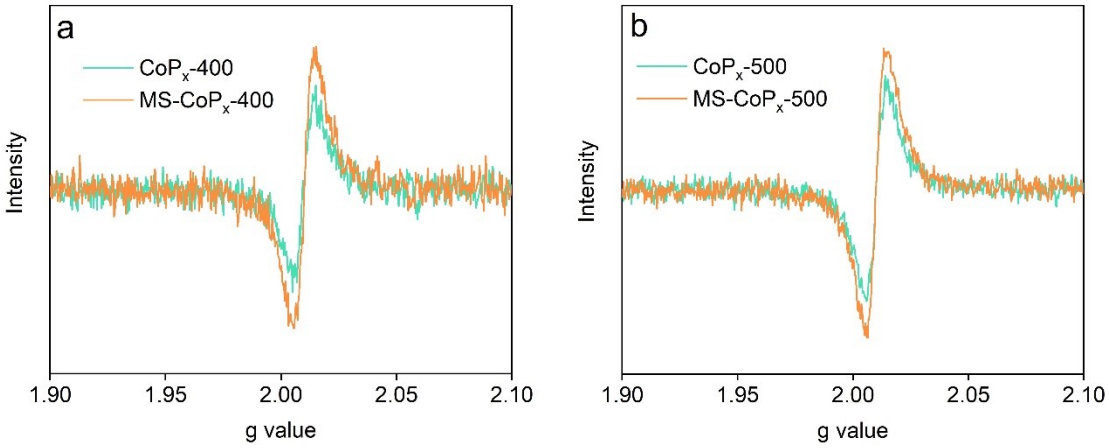

Fig. S8 EPR spectra of (a) CoP_x-400 and MS-CoP_x-400, (b) CoP_x-500 and MS-CoP_x-500.

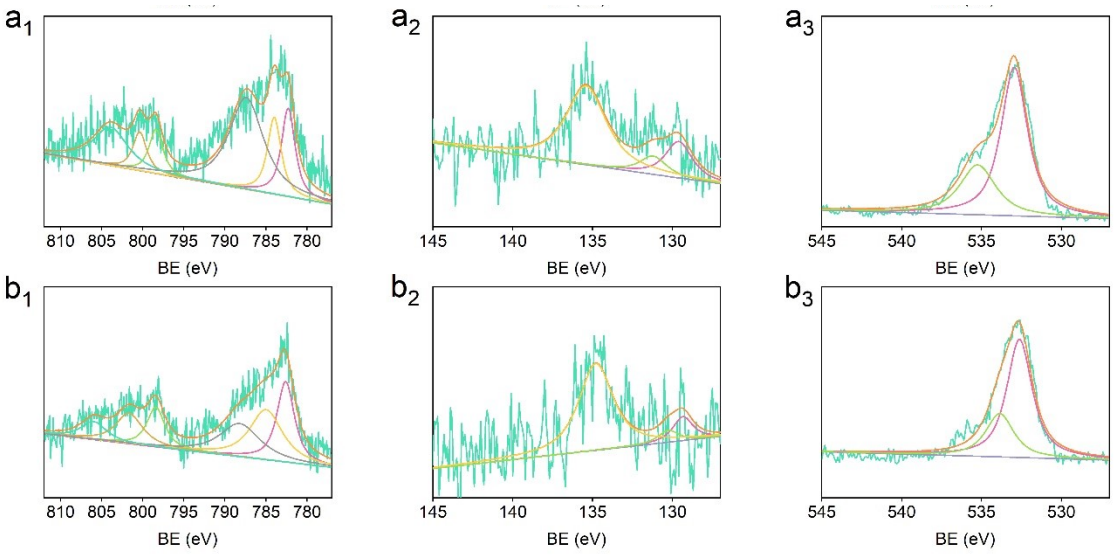

Fig. S9 XPS spectra of CoP_x-400 and CoP_x-500. (a_1-a_3) Co 2p, P 2p and O 1s high-resolution XPS spectra of CoP_x-400; (b_1-b_3) Co 2p, P 2p and O 1s high-resolution XPS spectra of CoP_x-500.

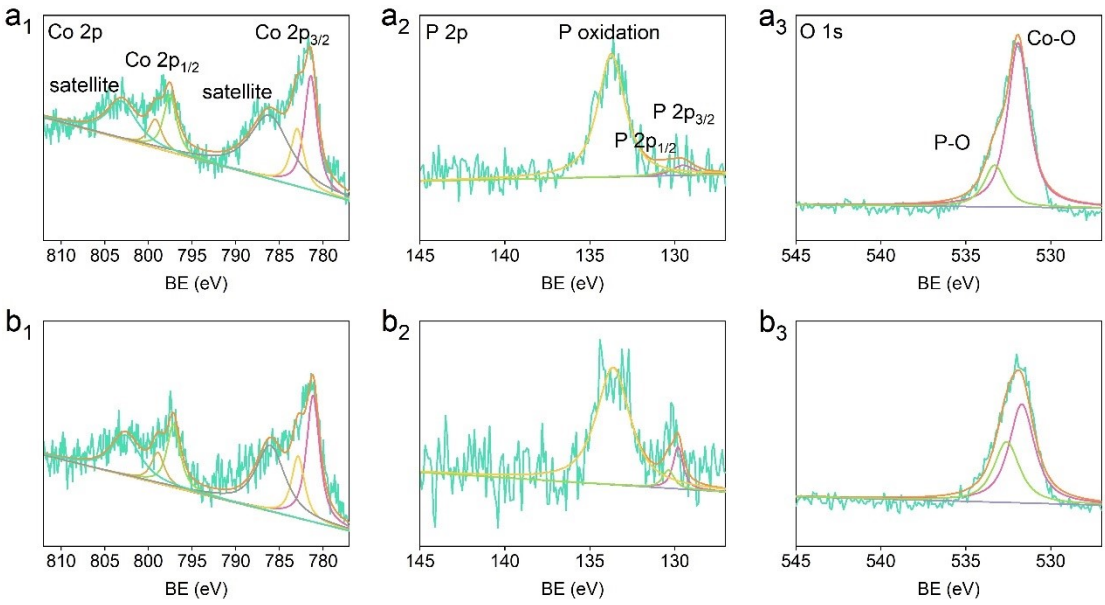

Fig. S10 XPS spectra of MS-CoP$_x$-400 and MS-CoP$_x$-500. (a_1-a_3) Co 2p, P 2p and O 1s high-resolution XPS spectra of MS-CoP$_x$-400; (b_1-b_3) Co 2p, P 2p and O 1s high-resolution XPS spectra of MS-CoP$_x$-500.

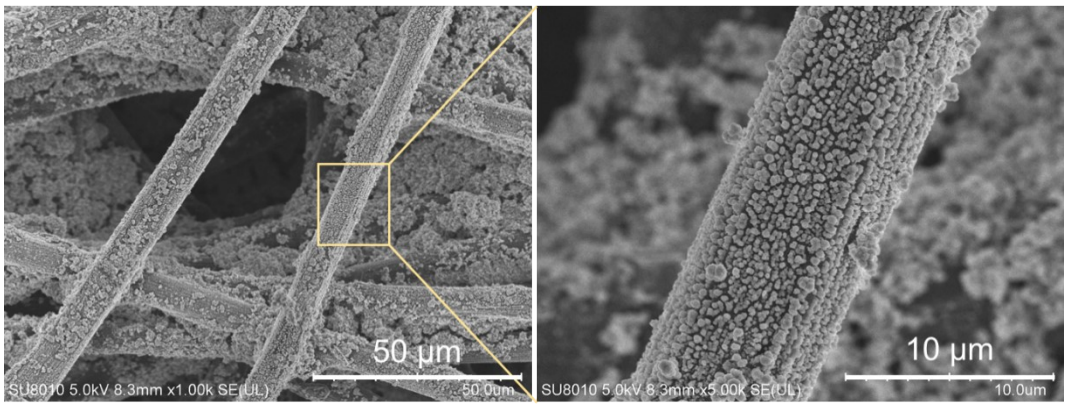

Fig. S11 SEM images of CoP_x supported on CFP.

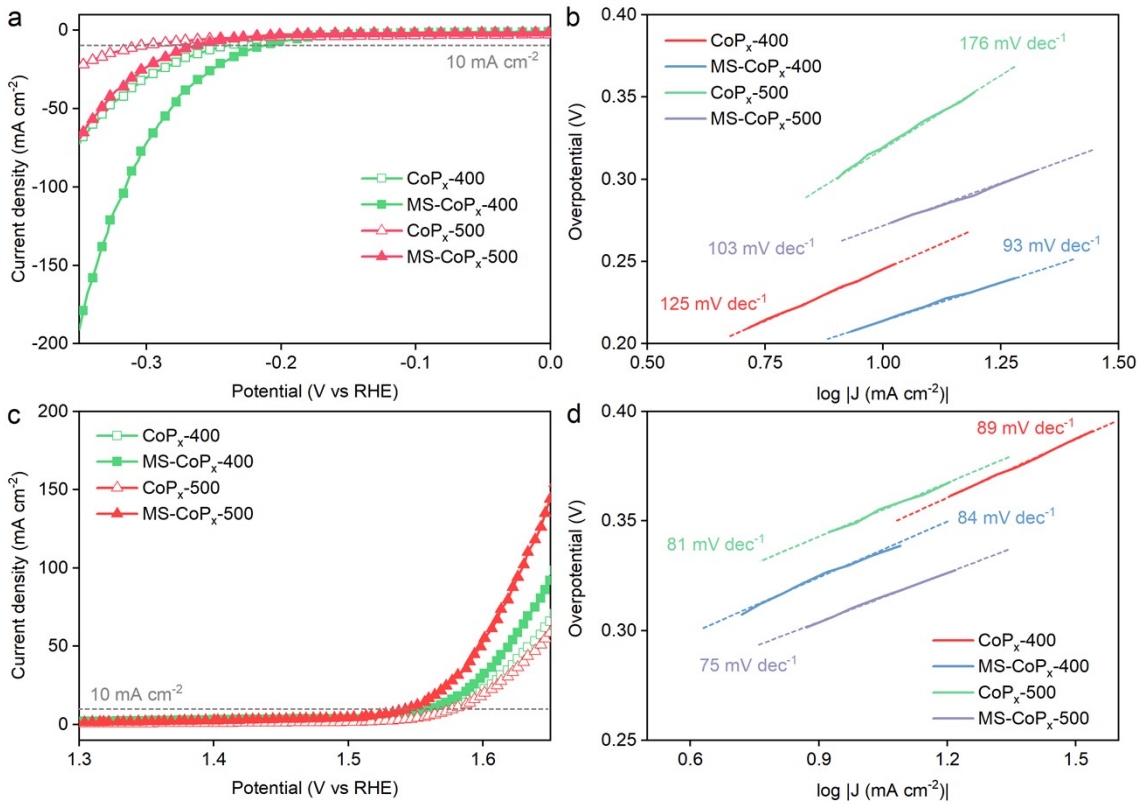

Fig. S12 Catalytic activity comparison of CoP_x prepared within or without molten salt under 400 and 500 °C. (a) HER polarization curves, (b) HER Tafel slopes, (c) OER polarization curves, (d) OER Tafel slopes. All measurements were carried out within a standard three-electrode configuration in N_2-saturated 1 M KOH. Graphite rod and Ag/AgCl served as the counter and reference electrode, respectively.

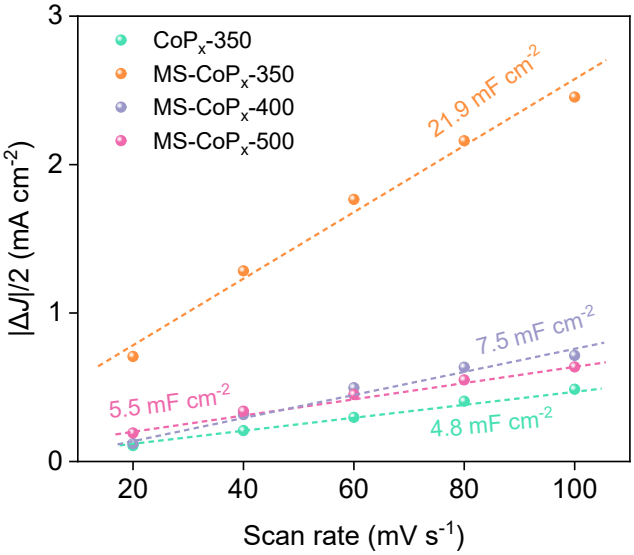

Fig. S13 Electrochemical active surface area calculated from cyclic voltammograms measured with varying scanning rates.

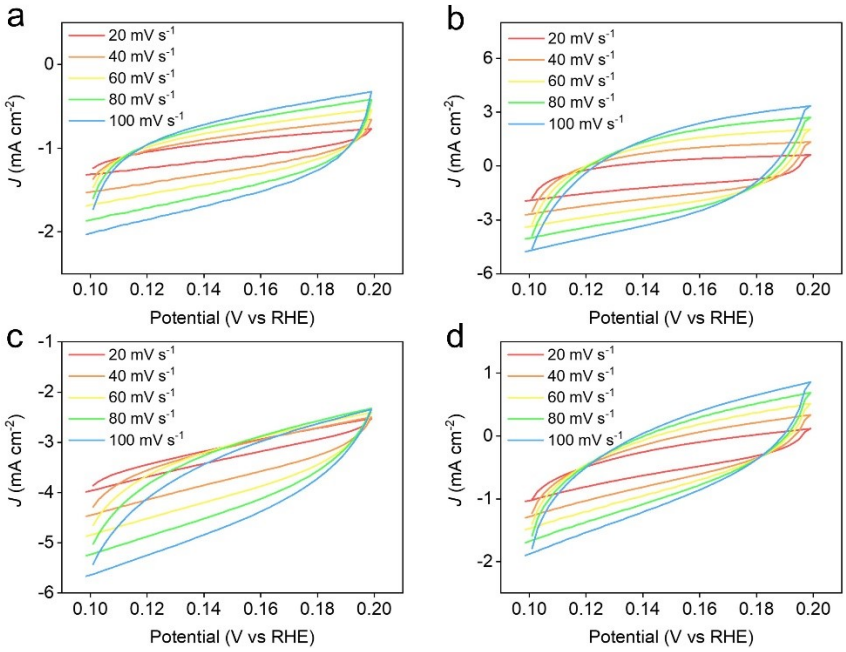

Fig. S14 Cyclic voltammograms measured with scanning rates of 20, 40, 60, 80 and 100 mV s^{-1}. (a) CoP_x-350, (b) MS-CoP_x-350, (c) MS-CoP_x-400, (d) MS-CoP_x-500.

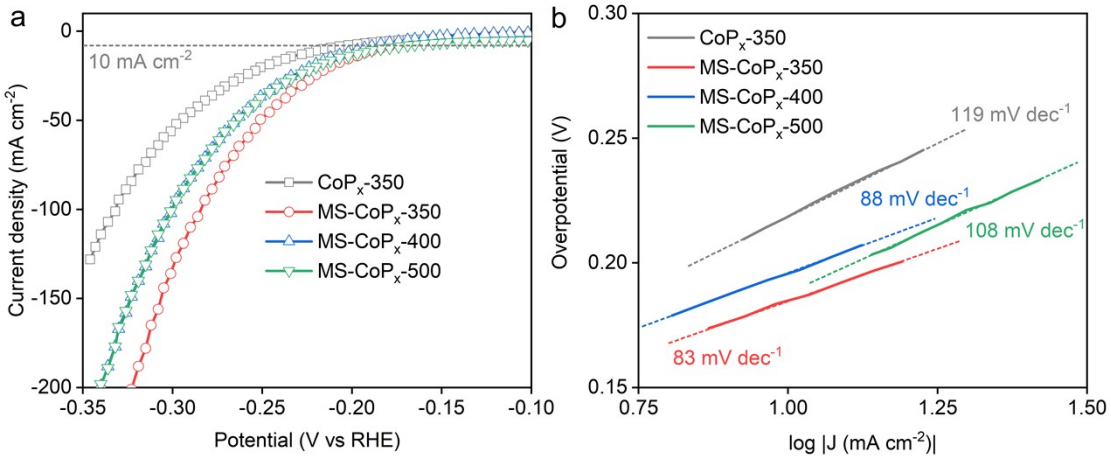

Fig. S15 Polarization curves and corresponding Tafel slopes of CoP_x toward HER in 0.5 M H_2SO_4 electrolyte. The measurements were conducted within a typical three-electrode configuration, where Ag/AgCl and graphite rod were employed as the reference and counter electrode, respectively. Polarization curves were recorded with a scan rate of 5 mV s^{-1}.

HER activity of CoP_x was also tested in acidic electrolyte (0.5 M H_2SO_4). MS-CoP_x-350 shows superior HER activity with a smaller overpotential of ~183 mV at 10 mA cm^{-2} than CoP_x-350 (~218 mV), MS-CoP_x-400 (~197 mV) and MS-CoP_x-500 (~190 mV), respectively. This is caused by the higher phosphidation of MS-CoP_x-350, where P usually acts as the active site for HER in acidic electrolyte because of its negatively charged nature.[9, 10] MS-CoP_x-350 also has a smaller Tafel slope (83 mV dec^{-1}) than other samples (88-119 mV dec^{-1}) and thus shows the most favorable kinetics. Moreover, this Tafel slope value suggests that HER over MS-CoP_x-350 is still controlled by a Volmer-Heyrovsky mechanism.[11] The superior HER activity of MS-CoP_x-350 under both alkaline and acidic conditions reveals its great potential to serve as a pH-universal cathodic electrocatalyst to drive water splitting.

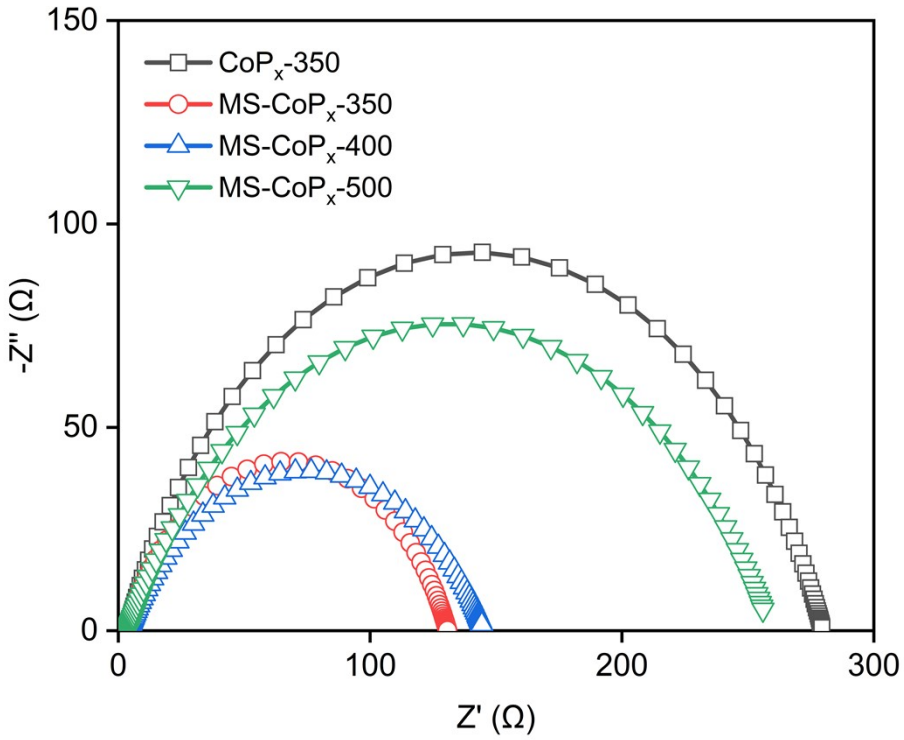

Fig. S16 EIS spectra of CoP_x measured in 0.5 M H_2SO_4 at the overpotential of 100 mV.

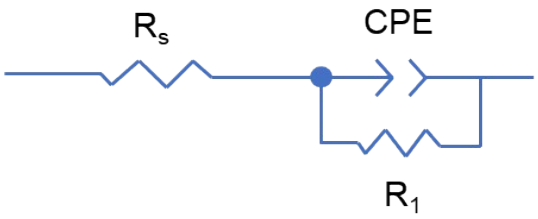

Fig. S17 Equivalent circuit model used for fitting the EIS spectra. R_s represent equivalent series resistance containing the contributions from electrolyte, catalyst itself and the electrical contact (lead) resistance. R_1 is related to the interface resistance, and CPE represents the constant phase element.

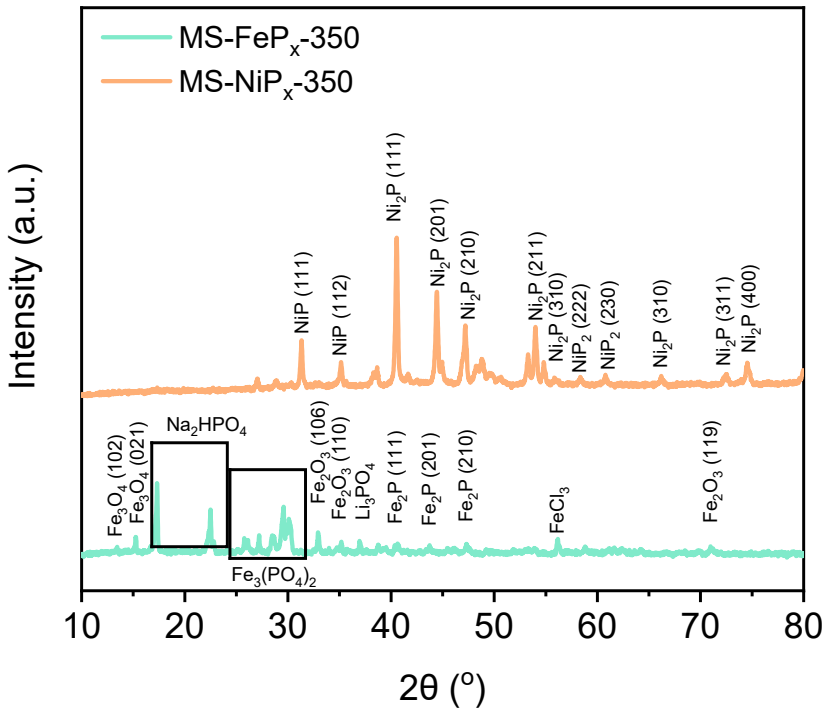

Fig. S18 XRD characterization of MS-FeP$_x$-350 and MS-NiP$_x$-350.

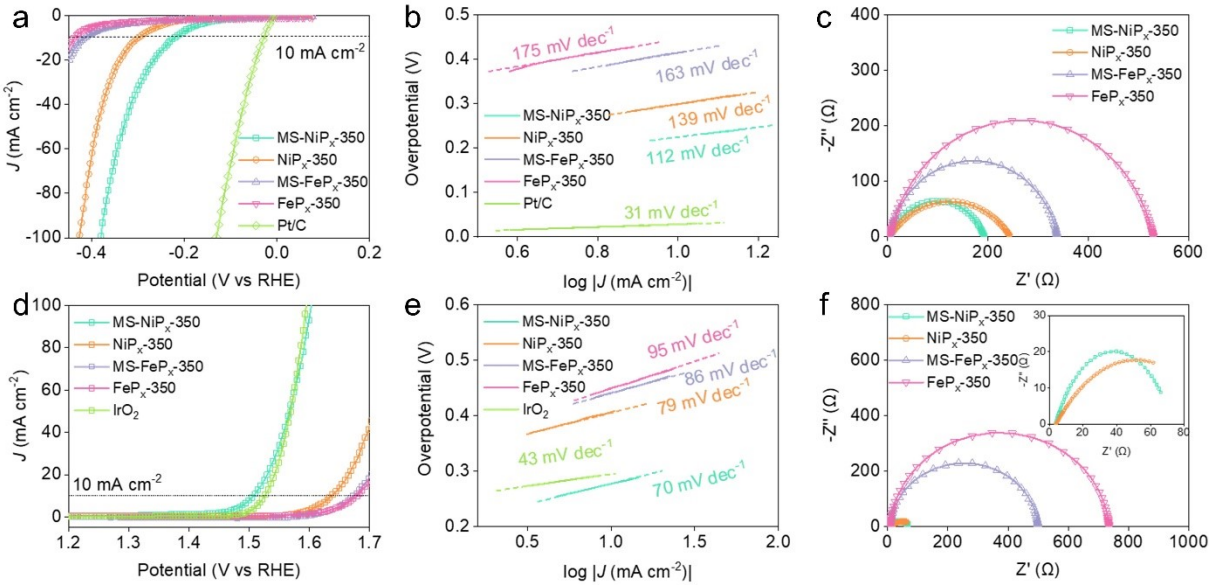

Fig. S19 Electrochemical measurements performed within a standard three-electrode configuration in 1 M KOH solution. (a-c) HER performance: (a) HER polarization curves, (b) Tafel slopes calculated from corresponding polarization curves, (c) Fitted electrochemical impedance spectra. (d-f) OER performance following the same sequence.

Electrochemical measurements of NiP_x and FeP_x were conducted under the same conditions as CoP_x. Polarization curves (Fig. S19, a and d) show that MS-NiP_x-350 has lower overpotentials (220 and 280 mV) compared to NiP_x-350 (298 and 410 mV) towards HER and OER (at 10 mA cm^{-2}), respectively. Tafel slopes were calculated from corresponding polarization curves to reveal the reaction kinetics (Fig. S19, b and e). Towards both HER and OER, MS-NiP_x-350 shows lower Tafel slopes (112 and 70 mV dec^{-1}, respectively) compared to NiP_x-350 (139 and 79 mV dec^{-1}, respectively), hence a faster reaction kinetic. It also suggests that both MS-NiP_x-350 and NiP_x-350 abide by Volmer-Heyrovsky HER pathway, wherein Volmer reaction is the rate-limiting step. We further measured the electrochemical impedance of MS-NiP_x-350 and NiP_x-350 during the HER and OER processes. Agreeing well with the polarization curves and Tafel slopes, MS-NiP_x-350 demonstrates smaller charge transfer resistance (R_{ct}) than NiP_x-350, as summarized by Table S9. All above results support the fact that molten salt medium endows NiP_x with higher catalytic activities. By comparison, due to the impurities and insufficient phosphidation, MS-FeP_x-350 and FeP_x-350 show much poorer catalytic activities when compared to MS-NiP_x-350 and NiP_x-350. Corresponding results were also presented in Fig. S19 and Table S9.

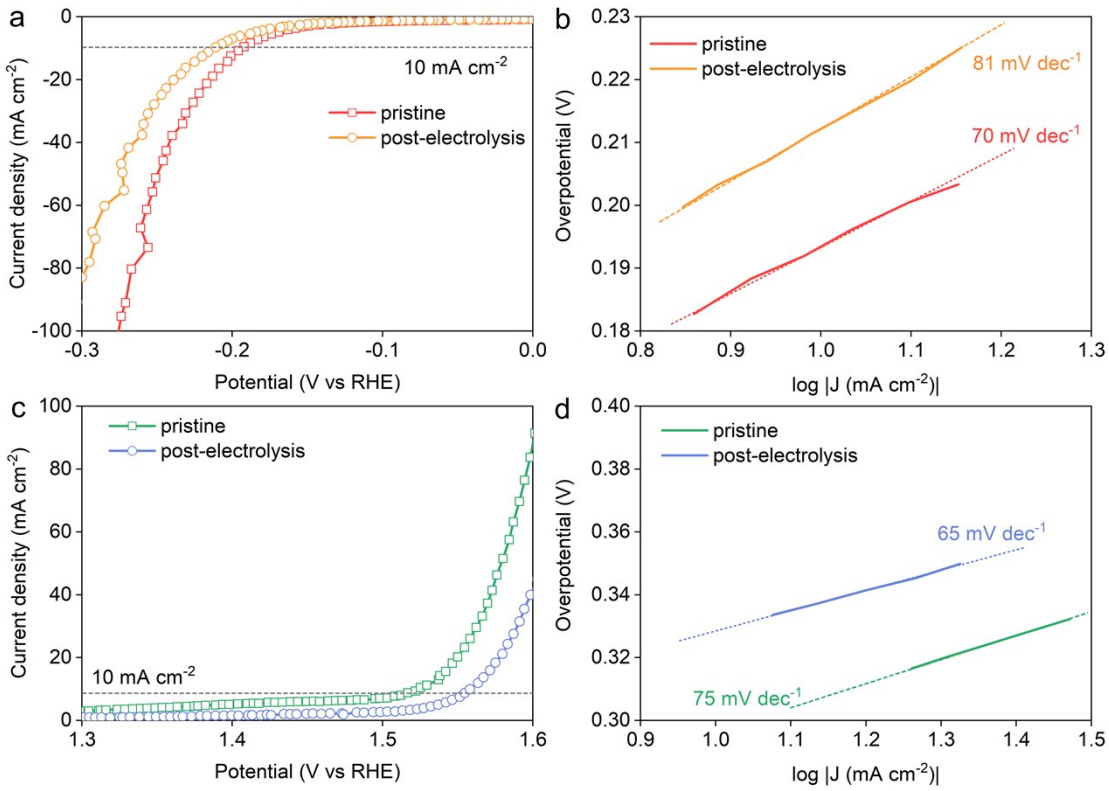

Fig. S20 Stability of MS-CoP$_x$-350 towards HER and OER in 1 M KOH. (a, b) HER activity of pristine and post-electrolysis MS-CoP$_x$-350. (c, d) OER activity of pristine and post-electrolysis MS-CoP$_x$-350. The stability was measured by running 1000 cycles' CV (HER, 0 to -0.5 V vs RHE; OER, 1.0 to 1.7 V vs RHE). The slight decay in performance is probably caused by the detachment of electrocatalysts from the CFP, because the Tafel slopes are still very similar before and after continuous CV running.

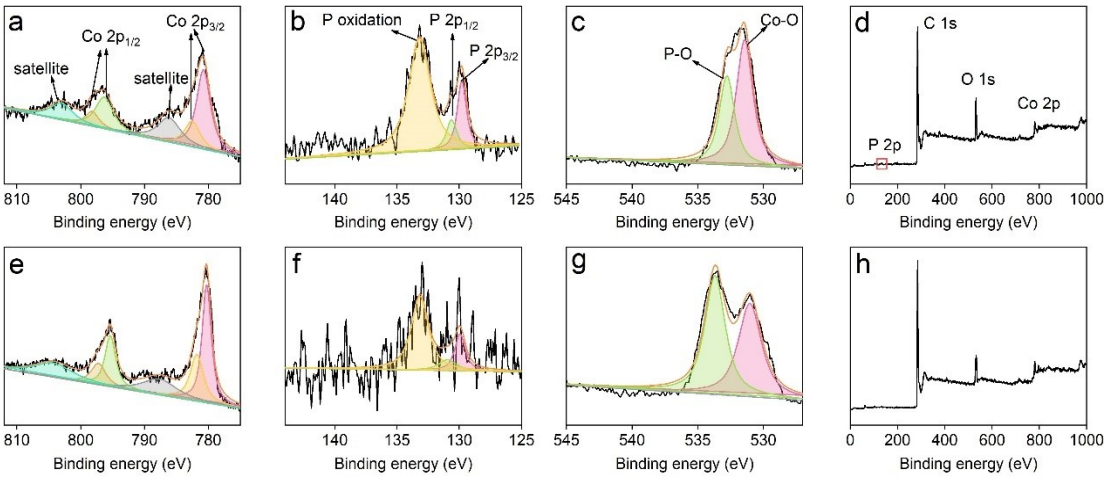

Fig. S21 XPS spectra of post-electrolysis MS-CoP$_x$-350. (a-d) Co 2p, P 2p, O 1s and survey spectra of post-HER MS-CoP$_x$-350. (e-h) Co 2p, P 2p, O 1s and survey spectra of post-OER MS-CoP$_x$-350.

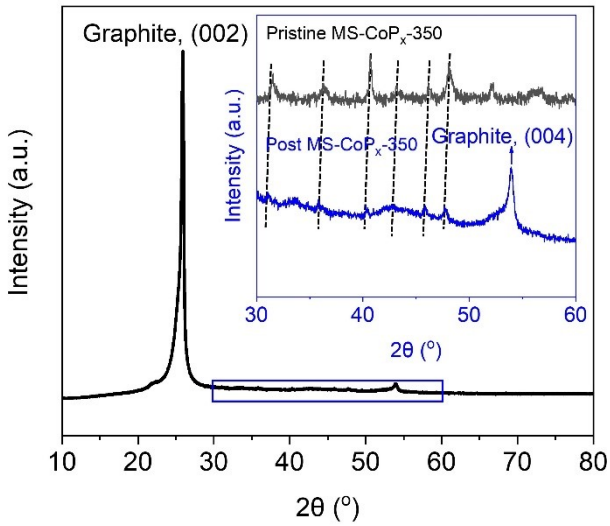

Fig. S22 XRD patterns of post-HER MS-CoP$_x$-350 supported on CFP subsequent to 24-hour electrolysis at 1.75 V cell voltage.

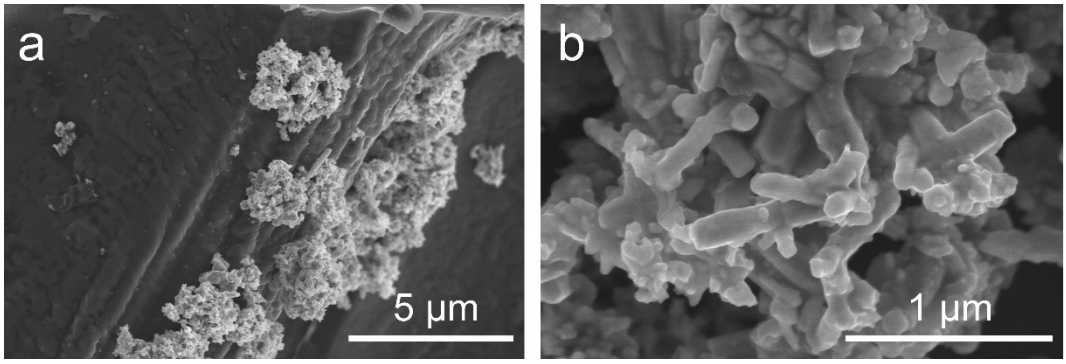

Fig. S23 SEM images of MS-CoP_x-350 supported on CFP subsequent to 24-hour electrolysis at 1.75 V cell voltage.

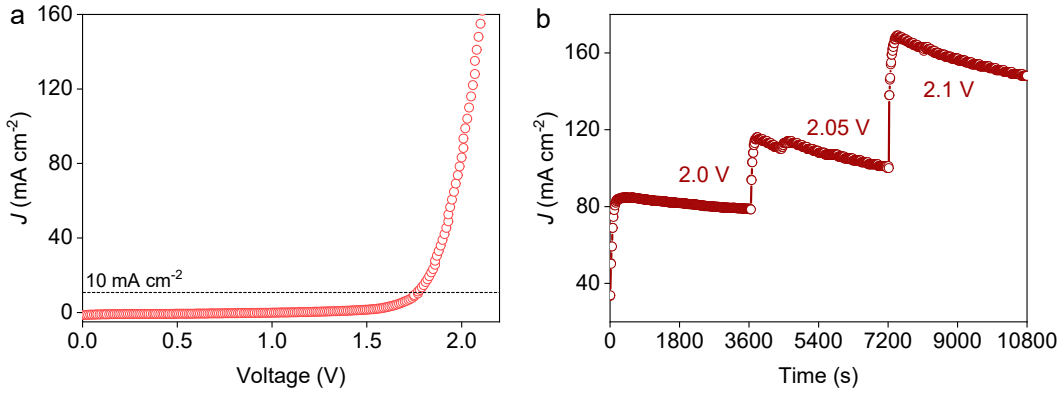

Fig. S24 Overall water splitting by MS-NiP$_x$-350||MS-NiP$_x$-350 electrolyzer in 1 M KOH solution. (a) Polarization curve of electrolyzer for overall water splitting; (b) Potentiostatic electrolysis by electrolyzer with varying cell voltages.

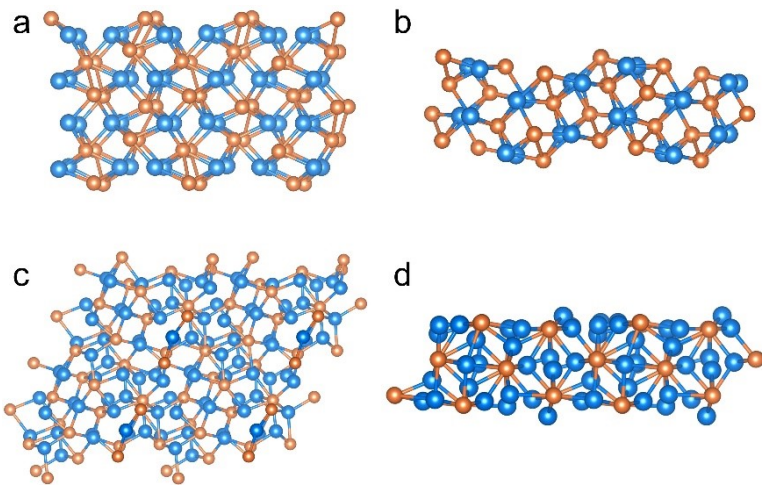

Fig. S25 Model structure constructed for DFT calculations. (a) Top view of CoP, (b) Side view of CoP, (c) Top view of Co_2P, (d) Side view of Co_2P.

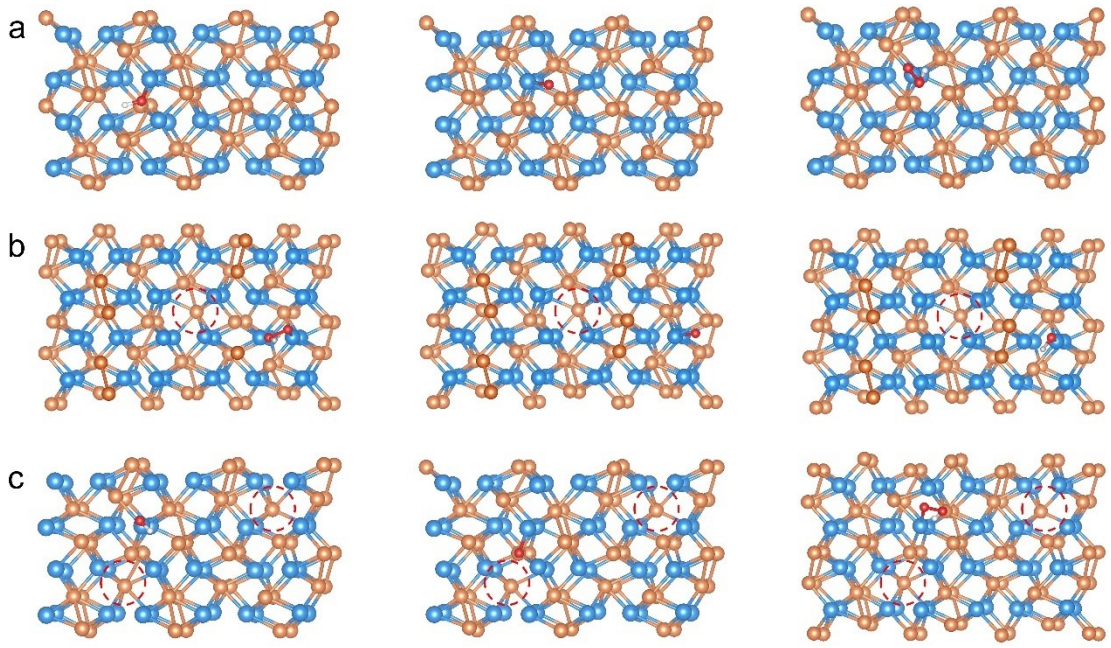

Fig. S26 Reaction coordinates adsorbed on (a) CoP, (b) CoP-PV1 and (c) CoP-PV2 during OER reaction. Adsorptions of OH*, O*, and OOH* on Co active site are shown from left to right.

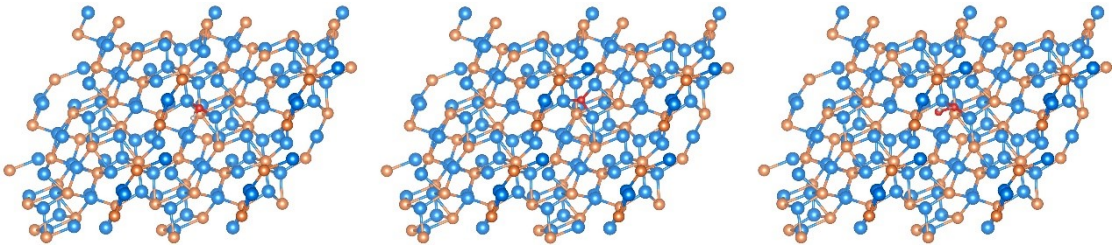

Fig. S27 Reaction coordinates adsorbed on Co_2P during OER reaction. Adsorptions of OH*, O*, and OOH* on Co active site are shown from left to right.

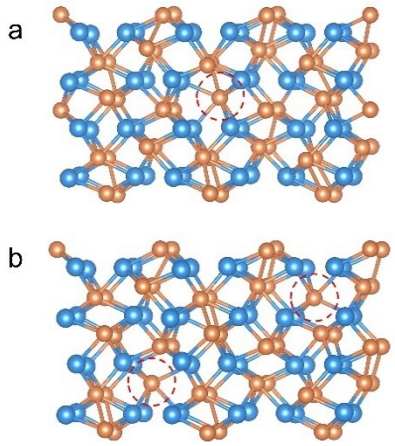

Fig. S28 Slab models for (a) CoP-PV1 and (b) CoP-PV2.

Table S1 Elemental composition of CoP_x detected by SEM-EDS

Sample	Element	Line	Atomic/%	Atomic ratio of P to Co
CoP_x-350	O	Ka	25.51	0.59
	P	Ka	27.76	
	Co	Ka	46.73	
CoP_x-400	O	Ka	15.18	0.40
	P	Ka	24.1	
	Co	Ka	60.72	
CoP_x-500	O	Ka	11.64	0.15
	P	Ka	11.56	
	Co	Ka	76.8	
MS-CoP_x-350	O	Ka	21.32	0.83
	P	Ka	35.76	
	Co	Ka	42.92	
MS-CoP_x-400	O	Ka	10.69	0.55
	P	Ka	31.62	
	Co	Ka	57.69	
MS-CoP_x-500	O	Ka	13.96	0.47
	P	Ka	27.55	
	Co	Ka	58.48	

The results presented in Table S1 show that: (i) higher temperature provides a lower phosphidation due to the faster evaporation of PH_3, and (ii) molten salt medium effectively enhances the phosphidation thanks to its space confinement effect.

Table S2 XRD patterns and corresponding planes and lattice spacings

Phase	2θ in standard PDF/°	Practical 2θ/°	Lattice spacing/Å	Plane
CoP	31.6	31.6	2.83	(011)
CoP	35.336	35.2	2.54	(200)
CoP	36.312	36.3	2.47	(111)
CoP	46.233	46.1	1.96	(112)
CoP	48.13	48.1	1.89	(211)
CoP	52.29	52.3	1.75	(103)
CoP	56.027	55.9	1.64	(020)
CoP	56.781	56.8	1.62	(301)
Co_2P	40.72	40.7	2.21	(121)
Co_2P	43.297	43.1	2.09	(211)

Table S3 XPS fitting of Co 2p, P 2p and corresponding assignment.

Sample	Peak type	Peak position eV	Peak assignments
CoP_x-350	Co $2p_{3/2}$	782.0	CoP_x
	Co $2p_{3/2}$	784.1	Co oxidation
	Co $2p_{1/2}$	798.0	CoP_x
	Co $2p_{1/2}$	800.9	Co oxidation
	Satellite	787.3	/
	Satellite	804.3	/
	P $2p_{3/2}$	128.5	CoP_x
	P $2p_{1/2}$	129.7	CoP_x
	P oxidation	134.6	P oxidation
CoP_x-400	Co $2p_{3/2}$	782.3	CoP_x
	Co $2p_{3/2}$	784.0	Co oxidation
	Co $2p_{1/2}$	798.4	CoP_x
	Co $2p_{1/2}$	800.4	Co oxidation
	Satellite	787.4	/
	Satellite	803.9	/
	P $2p_{3/2}$	129.6	CoP_x
	P $2p_{1/2}$	131.2	CoP_x
	P oxidation	135.4	P oxidation
CoP_x-500	Co $2p_{3/2}$	782.6	CoP_x
	Co $2p_{3/2}$	785.0	Co oxidation
	Co $2p_{1/2}$	798.4	CoP_x
	Co $2p_{1/2}$	801.6	Co oxidation
	Satellite	788.2	/
	Satellite	806.0	/
	P $2p_{3/2}$	129.3	CoP_x
	P $2p_{1/2}$	130.3	CoP_x
	P oxidation	134.8	P oxidation
MS-CoP_x-350	Co $2p_{3/2}$	781.39	CoP_x
	Co $2p_{3/2}$	783.44	Co oxidation
	Co $2p_{1/2}$	797.53	CoP_x
	Co $2p_{1/2}$	799.93	Co oxidation
	Satellite	787.19	/
	Satellite	804.19	/
	P $2p_{3/2}$	129.73	CoP_x
	P $2p_{1/2}$	130.36	CoP_x
	P oxidation	133.72	P oxidation
MS-CoP_x-400	Co $2p_{3/2}$	781.4	CoP_x
	Co $2p_{3/2}$	782.96	Co oxidation
	Co $2p_{1/2}$	797.5	CoP_x
	Co $2p_{1/2}$	799.2	Co oxidation
	Satellite	786.3	/
	Satellite	803.1	/
	P $2p_{3/2}$	129.5	CoP_x
	P $2p_{1/2}$	130.4	CoP_x
	P oxidation	133.72	P oxidation
MS-CoP_x-500	Co $2p_{3/2}$	781.2	CoP_x
	Co $2p_{3/2}$	782.86	Co oxidation
	Co $2p_{1/2}$	797.1	CoP_x
	Co $2p_{1/2}$	798.93	Co oxidation
	Satellite	786.03	/
	Satellite	802.63	/
	P $2p_{3/2}$	129.8	CoP_x
	P $2p_{1/2}$	130.36	CoP_x
	P oxidation	133.62	P oxidation

Table S4 Elemental composition of CoP_x detected by XPS

Sample	Element	Atomic/%	Atomic ratio of P to Co
CoP_x-350	O	78.75	0.52
	P	7.23	
	Co	14.02	
CoP_x-400	O	69.84	0.70
	P	12.46	
	Co	17.70	
CoP_x-500	O	71.09	0.69
	P	11.79	
	Co	17.12	
MS-CoP_x-350	O	74.17	2.13
	P	17.57	
	Co	8.26	
MS-CoP_x-400	O	77.63	0.88
	P	10.45	
	Co	11.93	
MS-CoP_x-500	O	75.12	0.78
	P	10.88	
	Co	14.00	

As a surface chemistry technique, XPS revealed the surface chemical composition of CoP_x (Table S4). O becomes the dominant element in all samples with an atomic ratio of 70~80%, which can be attributed to the inevitable surface oxidation of CoP_x upon contact with air and the abundant O contained by the CFP support. One can also see that the atomic ratio of P to Co in CoP_x synthesized within molten salt follows the same order as the SEM-EDS results (Table S1). However, for CoP_x synthesized without molten salt, the results suggest that high temperature induces a higher phosphidation on CoP_x's surface. This can be explained by the differences in detection techniques: EDS acquires the overall elemental composition, while XPS only provides the surface information. Under higher temperature, the evaporation of PH_3 is faster and hence inner part of Co precursor shows a lower phosphidation extent, while for Co precursors' surface, the continuous PH_3 flow tends to render a relatively higher phosphidation extent.

Table S5 R_s and R_{ct} values obtained by fitting the impedance spectra of different samples (Fig. 3c) using the equivalent circuits displayed in Fig. S17.

Sample	R_s/Ω	R_{ct}/Ω
CoP_x-350	2.617	436.8
MS-CoP_x-350	3.481	187.5
MS-CoP_x-400	3.69	228.3
MS-CoP_x-500	2.548	277.4

Table S6 R_s and R_{ct} values obtained by fitting the impedance spectra of different samples (Fig. S16) using the equivalent circuits displayed in Fig. S17.

Sample	R_s	R_{ct}
CoP_x-350	3.655	276
MS-CoP_x-350	3.674	127.1
MS-CoP_x-400	3.817	141.5
MS-CoP_x-500	3.84	255.1

Table S7 R_s and R_{ct} values obtained by fitting the impedance spectra of different samples (Fig. 3f) using the equivalent circuits displayed in Fig. S17.

Sample	R_s/Ω	R_{ct}/Ω
CoP_x-350	3.789	81.36
MS-CoP_x-350	3.205	24.19
MS-CoP_x-400	3.636	54.83
MS-CoP_x-500	3.379	32.5

Table S8 Comparison of the catalytic performance and synthetic strategy of CoP_x with other available CoP- and Co_2P-based electrocatalysts

No	Catalyst	HER performance [a]	OER performance [a]	Synthetic strategy	Co precursor [c]	Steps	Ref
1	MS-CoP_x-350	190	300	MSMP	$CoSO_4 \cdot 7H_2O$	1	This work
2	CoP	155	418	hydrothermal and vapor-phase phosphidation	$Co(OH)_2$	2	*Langmuir*, 2020, **36**, 1916-1922[12]
3	CoP NP	236	470	annealing and vapor-phase phosphidation	Co_3O_4	2	*Mater. Today Energy*, 2019, **12**, 443-452[13]
4	CoP	152	350	annealing and vapor-phase phosphidation	Co_3O_4	2	*Appl. Catal. B. Environ.*, 2021, **298**, 120488[14]
5	BP/Co_2P	~270	~400	wet chemistry and hydrothermal	$Co(acac)_2$	2	*Angew. Chem. Int. Ed.*, 2018, **57**, 2600-2604[15]
6	CoP NFs	136	323	precipitation, chemical etching, and vapor-phase phosphidation	Co-Co PBA NFs	3	*ACS Catal.*, 2020, **10**, 412-419[16]
7	CoP/NF	141.2	326@20 mA cm^{-2}	hydrothermal and vapor-phase phosphidation	$Co(OH)_2$	2	*Nano Res.*, 2021, **14**, 4173-4181[17]
8	Co_2P	150	330	hydrothermal and vapor-phase phosphidation	$Co(OH)_2$	2	*Nano Res.*, 2016, **9**, 2251-2259[18]
9	CoP	122	340	hydrothermal and vapor-phase phosphidation	$Co(OH)_2$	2	*Adv. Funct. Mater.*, 2020, **30**, 1909618[19]
10	CoP/CC	290	302	hydrothermal and vapor-phase phosphidation	Co_3O_4	2	*ACS Catal.*, 2017, **7**, 4131-4137[20]

[a] HER and OER performance was evaluated by the required overpotential to reach 10 mA cm^{-2} if not specified.

Table S9 Electrochemical results summarization of Fe- and Ni- based electrocatalysts during HER and OER processes

Sample	Reaction	Overpotential @10 mA cm^{-2}	Tafel slope mV dec^{-1}	R_s/Ω	R_{ct}/Ω
MS-NiP_x-350	HER	220	112	3.85	192.6
	OER	280	70	3.92	69.0
NiP_x-350	HER	298	139	4.93	240.9
	OER	410	79	3.98	72.1
MS-FeP_x-350	HER	414	163	4.46	334.9
	OER	440	86	4.28	491.4
FeP_x-350	HER	436	175	4.85	525.5
	OER	450	95	5.32	728.0

Table S10 Comparison of the binding energy positions of Co 2p and P 2p in pristine MS-CoP_x-350, post-HER MS-CoP_x-350 and post-OER MS-CoP_x-350.

Sample	Peak type	Peak position eV	Peak assignments
Pristine MS-CoP_x-350	Co $2p_{3/2}$	781.39	CoP_x
	Co $2p_{3/2}$	783.44	Co oxidation
	Co $2p_{1/2}$	797.53	CoP_x
	Co $2p_{1/2}$	799.93	Co oxidation
	Satellite	787.19	/
	Satellite	804.19	/
	P $2p_{3/2}$	129.73	CoP_x
	P $2p_{1/2}$	130.36	CoP_x
	P oxidation	133.72	P oxidation
Post-HER MS-CoP_x-350	Co $2p_{3/2}$	780.78	CoP_x
	Co $2p_{3/2}$	782.54	Co oxidation
	Co $2p_{1/2}$	796.32	CoP_x
	Co $2p_{1/2}$	798.2	Co oxidation
	Satellite	786.18	/
	Satellite	803	/
	P $2p_{3/2}$	129.8	CoP_x
	P $2p_{1/2}$	130.63	CoP_x
	P oxidation	133.19	P oxidation
Post-OER MS-CoP_x-350	Co $2p_{3/2}$	780.28	CoP_x
	Co $2p_{3/2}$	781.82	Co oxidation
	Co $2p_{1/2}$	795.37	CoP_x
	Co $2p_{1/2}$	797.22	Co oxidation
	Satellite	787.66	/
	Satellite	804.25	/
	P $2p_{3/2}$	129.94	CoP_x
	P $2p_{1/2}$	130.94	CoP_x
	P oxidation	133.17	P oxidation

Table S11 Overall water splitting performance of noble-metal-free electrocatalysts to produce 10 mA cm^{-2}

Catalysts	Cell voltage/V	Electrolyte	Ref
MS-CoP_x-350	~1.75	1 M KOH	This work
Co_2P/Co-foil	1.71	1 M KOH	*J. Mater. Chem. A* 2017, 5, 10561-10566[21]
Co-P/NC	1.71	1 M KOH	Chem. Mater. 2015, 27, 7636-7642[22]
Fe-Ni@NC-CNTs	~1.8	1 M KOH	*Angew. Chem. Int. Ed.* 2018, 57, 8921-8926[23]
Mo_2C/CS	1.73	1 M KOH	*ChemSusChem* 2017, 10, 3540-3546[24]
β-$Ni(OH)_2$/$NiSe_2$ nanosheets	1.78	1 M KOH	*Chem. Mater.* 2015, 27, 5702-5711[25]
CoP/rGO-400	1.7	1 M KOH	*Chem. Sci.* 2016, 7, 1690-1695[26]
CoMnCH/NF	1.68	1 M KOH	*J. Am. Chem. Soc.* 2017, 139, 8320-8328[27]
BP/Co_2P	1.92	1 M KOH	*Angew. Chem. Int. Ed.* 2018, 57, 2600-2604[15]
PPy/FeTCPP/Co	1.81	0.1 M KOH	*Adv. Funct. Mater.* 2017, 27, 1606497[28]
AlNi-LDH	1.56	1 M KOH	*ACS Energy Lett.* 2018, 3, 892-898[29]

References

1. D. Q. Yang and E. Sacher, s–p Hybridization in highly oriented pyrolytic graphite and its change on surface modification, as studied by X-ray photoelectron and Raman spectroscopies, *Surf. Sci.*, 2002, **504**, 125-137.
2. C. M. Gabardo, C. P. O'Brien, J. P. Edwards, C. McCallum, Y. Xu, C.-T. Dinh, J. Li, E. H. Sargent and D. Sinton, Continuous Carbon Dioxide Electroreduction to Concentrated Multi-carbon Products Using a Membrane Electrode Assembly, *Joule*, 2019, **3**, 2777-2791.
3. G. Kresse and J. Furthmüller, Efficiency of ab-initio total energy calculations for metals and semiconductors using a plane-wave basis set, *Comput. Mater. Sci.*, 1996, **6**, 15-50.
4. G. Kresse and J. Furthmüller, Efficient iterative schemes for ab initio total-energy calculations using a plane-wave basis set, *Phys. Rev. B*, 1996, **54**, 11169-11186.
5. J. P. Perdew, K. Burke and M. Ernzerhof, Generalized Gradient Approximation Made Simple, *Phys. Rev. Lett.*, 1996, **77**, 3865-3868.
6. G. Kresse and D. Joubert, From ultrasoft pseudopotentials to the projector augmented-wave method, *Phys. Rev. B*, 1999, **59**, 1758-1775.
7. H. J. Monkhorst and J. D. Pack, Special points for Brillouin-zone integrations, *Phys. Rev.*

B, 1976, **13**, 5188-5192.

8. Z. Zhao and Z. Xia, Design Principles for Dual-Element-Doped Carbon Nanomaterials as Efficient Bifunctional Catalysts for Oxygen Reduction and Evolution Reactions, *ACS Catal.*, 2016, **6**, 1553-1558.
9. F. H. Saadi, A. I. Carim, E. Verlage, J. C. Hemminger, N. S. Lewis and M. P. Soriaga, CoP as an Acid-Stable Active Electrocatalyst for the Hydrogen-Evolution Reaction: Electrochemical Synthesis, Interfacial Characterization and Performance Evaluation, *J. Phys. Chem. C*, 2014, **118**, 29294-29300.
10. X. Xiao, L. Tao, M. Li, X. Lv, D. Huang, X. Jiang, H. Pan, M. Wang and Y. Shen, Electronic modulation of transition metal phosphide via doping as efficient and pH-universal electrocatalysts for hydrogen evolution reaction, *Chem. Sci.*, 2018, **9**, 1970-1975.
11. Y. Shi and B. Zhang, Recent advances in transition metal phosphide nanomaterials: synthesis and applications in hydrogen evolution reaction, *Chem. Soc. Rev.*, 2016, **45**, 1529-1541.
12. L. Li, X. Wang, Y. Guo and J. Li, Synthesis of an Ultrafine CoP Nanocrystal/Graphene Sandwiched Structure for Efficient Overall Water Splitting, *Langmuir*, 2020, **36**, 1916-1922.
13. L. Yan, S. Zhao, Y. Li, B. Zhang, J. Zhu, Z. Liu, X. Yuan, J. Yu, H. Zhang and P. K. Shen, Hierarchical cobalt phosphide hollow nanoboxes as high performance bifunctional electrocatalysts for overall water splitting, *Mater. Today Energy*, 2019, **12**, 443-452.
14. Y. Song, J. Cheng, J. Liu, Q. Ye, X. Gao, J. Lu and Y. Cheng, Modulating electronic structure of cobalt phosphide porous nanofiber by ruthenium and nickel dual doping for highly-efficiency overall water splitting at high current density, *Appl. Catal. B: Environ.*, 2021, **298**, 120488.
15. J. Wang, D. Liu, H. Huang, N. Yang, B. Yu, M. Wen, X. Wang, P. K. Chu and X.-F. Yu, In-Plane Black Phosphorus/Dicobalt Phosphide Heterostructure for Efficient

Electrocatalysis, *Angew. Chem. Int. Ed.*, 2018, **57**, 2600-2604.

16. L. Ji, J. Wang, X. Teng, T. J. Meyer and Z. Chen, CoP Nanoframes as Bifunctional Electrocatalysts for Efficient Overall Water Splitting, *ACS Catal.*, 2020, **10**, 412-419.
17. H. Xue, A. Meng, H. Zhang, Y. Lin, Z. Li and C. Wang, 3D urchin like V-doped CoP in situ grown on nickel foam as bifunctional electrocatalyst for efficient overall water-splitting, *Nano Res.*, 2021, **14**, 4173-4181.
18. Y. Li, H. Zhang, M. Jiang, Y. Kuang, X. Sun and X. Duan, Ternary NiCoP nanosheet arrays: An excellent bifunctional catalyst for alkaline overall water splitting, *Nano Res.*, 2016, **9**, 2251-2259.
19. L. Yang, R. Liu and L. Jiao, Electronic Redistribution: Construction and Modulation of Interface Engineering on CoP for Enhancing Overall Water Splitting, *Adv. Funct. Mater.*, 2020, **30**, 1909618.
20. C. Du, L. Yang, F. Yang, G. Cheng and W. Luo, Nest-like NiCoP for Highly Efficient Overall Water Splitting, *ACS Catal.*, 2017, **7**, 4131-4137.
21. C.-Z. Yuan, S.-L. Zhong, Y.-F. Jiang, Z. K. Yang, Z.-W. Zhao, S.-J. Zhao, N. Jiang and A.-W. Xu, Direct growth of cobalt-rich cobalt phosphide catalysts on cobalt foil: an efficient and self-supported bifunctional electrode for overall water splitting in alkaline media, *J. Mater. Chem. A*, 2017, **5**, 10561-10566.
22. B. You, N. Jiang, M. Sheng, S. Gul, J. Yano and Y. Sun, High-Performance Overall Water Splitting Electrocatalysts Derived from Cobalt-Based Metal–Organic Frameworks, *Chem. Mater.*, 2015, **27**, 7636-7642.
23. X. Zhao, P. Pachfule, S. Li, J. R. J. Simke, J. Schmidt and A. Thomas, Bifunctional Electrocatalysts for Overall Water Splitting from an Iron/Nickel-Based Bimetallic Metal–Organic Framework/Dicyandiamide Composite, *Angew. Chem. Int. Ed.*, 2018, **57**, 8921-8926.
24. H. Wang, Y. Cao, C. Sun, G. Zou, J. Huang, X. Kuai, J. Zhao and L. Gao, Strongly

Coupled Molybdenum Carbide on Carbon Sheets as a Bifunctional Electrocatalyst for Overall Water Splitting, *ChemSusChem*, 2017, **10**, 3540-3546.

25. H. Liang, L. Li, F. Meng, L. Dang, J. Zhuo, A. Forticaux, Z. Wang and S. Jin, Porous Two-Dimensional Nanosheets Converted from Layered Double Hydroxides and Their Applications in Electrocatalytic Water Splitting, *Chem. Mater.*, 2015, **27**, 5702-5711.
26. L. Jiao, Y.-X. Zhou and H.-L. Jiang, Metal–organic framework-based CoP/reduced graphene oxide: high-performance bifunctional electrocatalyst for overall water splitting, *Chem. Sci.*, 2016, **7**, 1690-1695.
27. T. Tang, W.-J. Jiang, S. Niu, N. Liu, H. Luo, Y.-Y. Chen, S.-F. Jin, F. Gao, L.-J. Wan and J.-S. Hu, Electronic and Morphological Dual Modulation of Cobalt Carbonate Hydroxides by Mn Doping toward Highly Efficient and Stable Bifunctional Electrocatalysts for Overall Water Splitting, *J. Am. Chem. Soc.*, 2017, **139**, 8320-8328.
28. J. Yang, X. Wang, B. Li, L. Ma, L. Shi, Y. Xiong and H. Xu, Novel Iron/Cobalt-Containing Polypyrrole Hydrogel-Derived Trifunctional Electrocatalyst for Self-Powered Overall Water Splitting, *Adv. Funct. Mater.*, 2017, **27**, 1606497.
29. Z. Li, W. Niu, L. Zhou and Y. Yang, Phosphorus and Aluminum Codoped Porous NiO Nanosheets as Highly Efficient Electrocatalysts for Overall Water Splitting, *ACS Energy Lett.*, 2018, **3**, 892-898.